# Polarization-dependent electronic structure of Ag quantum well states on the $MoS_2(0001)$ surface using ARPES and DFT studies

Arunava Kar,[1] Sanjoy Kr Mahatha,[2,*] and Krishnakumar S. R. Menon[1,†]
[1]*Surface Physics and Material Science Division, Saha Institute of Nuclear Physics, A CI of Homi Bhabha National Institute, 1/AF Bidhannagar, Kolkata 700064, India*
[2]*UGC-DAE Consortium for Scientific Research, Khandwa Road, Indore, Madhya Pradesh 452001, India*

(Received 21 October 2022; revised 6 December 2022; accepted 12 December 2022; published 22 December 2022)

The electronic band structure of clean and Ag-induced quantum well states on the $MoS_2(0001)$ surface has been investigated using polarization-dependent angle-resolved photoemission spectroscopy (ARPES) along with first-principle-based density functional theory (DFT) calculations. Using selective linearly polarized light, the orbital symmetry and $k$ dispersion of the surface localized electronic states have been unambiguously determined. The quantum well states (QWS) originating from the Ag $p_z$ orbitals are confined within the Ag overlayer, while the quantum well resonance states (QWRS) are hybridized with substrate Mo $4d_{z^2}$ and S $3p_z$ orbitals. The photon energy dependence of the dispersion characteristics confirms the two-dimensional (2D) nature of these quantum states while their momentum dependence is a consequence of the finite lateral coherence length of the electrons. Our ARPES experiments using incident circularly polarized light on $MoS_2(0001)$ surface show circular dichroism effects (CD-ARPES), similar to recent studies where it is used to probe the initial state orbital angular momentum or the Berry curvature. While the QWS on the Ag overlayer does not exhibit any intensity asymmetry with the helicity of the incident light, the Ag QWRS show circular dichroism characteristics. The observed circular dichroism from the QWRS is attributed to the hybridization of these quantum states to the substrate states. We compare our ARPES results with the calculated orbital projected band structure to obtain a microscopic insight into the electronic behavior, which is critically important for manipulating wave functions for potential device applications.

DOI: 10.1103/PhysRevB.106.235146

## I. INTRODUCTION

After the discovery of graphene and topological insulators, there have been an outburst of research activities on 2D materials to understand their physical properties and find applications to the next-generation optoelectronic and spintronic devices [1–3]. One class of 2D materials that are getting more attention in recent days is the transition metal dichalcogenides (TMDCs) family as a monolayer or a few layers of $MX_2$ (e.g., M = Ti, V, Nb, Ta, Mo, W and X = S, Se, Te) [4–6]. These materials are very easy to exfoliate and fabricate devices as their interlayers are coupled with weak van der Waals (vdW) forces. When isolated atomic planes are stacked in a layer-by-layer fashion, bounded by weak vdW forces, they exhibit unusual properties and phenomena which are very different from those of their bulk counterparts [5]. Furthermore, these 2D materials also offer greater flexibility in tuning their electronic properties through band-gap engineering which can be carried out by changing the number of layers of the material [7,8].

Among the layered 2D-TMDCs, molybdenum disulfide ($MoS_2$) is the most studied material as a potential candidate for future nanoscale device applications [9–12]. $MoS_2$ is an indirect band gap semiconductor (1.29 eV) that can be tuned from an indirect to a direct one upon reducing the size from bulk to monolayer [7]. The presence of the band gap makes $MoS_2$ remarkably suitable for potential thin film transistor applications over gapless graphene [13]. More strikingly, it is observed that bulk $MoS_2$ exhibits hidden valley and layer-locked spin-polarized electronic states [14], while monolayer $MoS_2$ exhibits exotic spin-valley coupling phenomena that make it appropriate for spintronics and valleytronics devices applications [15]. The key limiter to the electronic performances of these 2D semiconductor devices is the metal contact which affects its electronic, phononic, and transport properties [16–18]. Though many experimental studies demonstrate the practical applications of $MoS_2$-based devices [3,9,19,20], the key aspect of the electronic structure evolution under external effects such as doping, deposition, or heterostructuring is little explored in the literature. Metallic thin films in contact with $MoS_2$ exhibit a remarkable effect of electron confinement within the film forming the quantum well states (QWS) [21]. This quantum confinement could potentially enhance the optoelectronic performances of the system and be utilized in optoelectronic device applications [22]. Effect of the underlying substrate bands also have a significant effect on the electronic properties of the overlayer QWS such as in-plane effective mass enhancement, splitting of the quantum states [23,24], etc. The QWS associated with the spin states at the substrate interface can provide a magnetic coupling channel through the noble metal which also has potential applications in magnetic and magneto-optic storage and spintronic devices [25,26]. Furthermore, for the spintronic

*sanjoymahatha@gmail.com
†Corresponding author: krishna.menon@saha.ac.in

 

applications, manipulating the wave functions is also important to achieve select spin configurations. Therefore, studying the orbital texture of the wave functions and its coupling to the spin texture is indispensable for both the understanding of the inherent fundamental physics as well as for their potential applications.

ARPES offers an exclusive opportunity to directly probe the $k$-state orbital texture with different symmetries through the utilization of photon polarization selection rules [27]. The measured intensity ($I$) of an ARPES experiment strongly depends on the transition matrix elements of the photoemission process and can be expressed as $I \propto \langle \Psi_f | \vec{A} \cdot \vec{p} | \Psi_i \rangle$, where $\vec{A}$ is the electromagnetic gauge and $\vec{p}$ is the electron momentum. $\vec{A}$ exhibits the same spatial mirror symmetry as the electric field ($\vec{E}$) of the incident polarized photon beam while $|\Psi_i\rangle$ and $|\Psi_f\rangle$ are the electron wave function in solid (initial state) and the wave function of the excited photoelectron (final state), respectively [28,29]. The initial state wave function contains all the information on the orbital symmetry of the electrons within a solid while the final state wave function can be described by a plane wave traveling to the photoelectron analyzer. For a linearly polarized electric field, only a particular symmetry of the initial states $|\Psi_i\rangle$ contributes to the intensity while other symmetries do not contribute as the "matrix element" integrates over all the spatial dimensions, and if the parity products of $\langle \Psi_f | \vec{A} \cdot \vec{p} | \Psi_i \rangle$ is overall odd with respect to a concerning mirror plane, then the integration vanishes and the ARPES intensity becomes zero [28]. However, for circularly polarized light, the photoemission matrix element gets modified depending on the handedness of the incident photon and is used to probe the valley-selective circular dichroism [15] in layered TMDC materials. Circular dichroism (CD) in ARPES has recently been shown to bear information on the orbital angular momentum (OAM) and the Berry curvature of the spin-split initial states in systems without inversion symmetry [30,31]. For polarization-dependent photoemission studies, the proper arrangement of the experimental geometry is important which can determine the symmetry of the initial states based on the general photoemission selection rules and can compare them to the theoretical prediction of the orbital characteristics of the electronic bands for a deep understanding of the system.

In the present work we have used polarization-dependent ARPES experiments to explore and map the electronic band dispersions and their orbital textures for clean and Ag deposited $MoS_2(0001)$ surfaces along the $\bar{\Gamma}$-$\bar{K}$ symmetry direction. The Ag-covered $MoS_2(0001)$ surface exhibits a nearly free 2D electron gas within the Ag overlayers in the form of QWS. Our earlier studies of the thickness-dependent behavior of these QWS [21] showed the importance of the hybridization effects at the interface in these quantum states. Here we explore their orbital textures and interfacial hybridization characteristics with the support of density functional theory (DFT) calculations. The electronic band structure is found to be significantly different for the orbital states of even and odd reflection parities along the $\bar{\Gamma}$-$\bar{K}$ symmetry line even in the absence of a true mirror symmetry plane along this direction. Our ARPES experiments using circular polarized light on bare $MoS_2(0001)$ surface show a CD signal near $\bar{\Gamma}$ similar to the earlier reports [30,31]. Interestingly, the QWRS formed upon Ag deposition also show the CD signal due to the hybridization with the underlying substrate states while the QWS which are confined to the Ag film do not display any CD effects. Our experimental results together with the orbital projected band structure calculations provide a fundamental understanding of the electronic structure of the system.

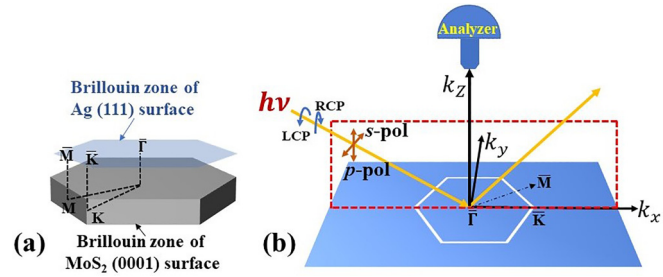


FIG. 1. (a) Schematic of the first Brillouin zone and the corresponding high-symmetry directions of the $MoS_2(0001)$ substrate surface and the overlayer Ag(111) surface. (b) Schematic of the experimental geometry for the photoemission experiment.

## II. METHODS

### A. Experimental details

ARPES experiments were carried out using linearly ($s$ and $p$) and left/right circularly polarized (LCP/RCP) photons at the low-energy branch of the APE beamline at Elettra Sincrotrone Trieste in the photon energy range of 35–90 eV [32] as well as using unpolarized monochromatic He $II_\alpha$ (40.8 eV) photons in laboratory [33]. Different degrees of polarization of the highly intense photon beams were obtained in the Apple II quasiperiodic undulator beamline by changing the undulator gap and phase differences. The circular polarization rate was estimated to be around 65% for both helicities with a little variation in photon energies and the size of the photon beam spot on the sample surface was $50 \times 150$ $\mu m^2$. The $p$ polarized incident light was not absolute and contains a maximum of about 6% incomplete $s$ polarized light [32,34]. Figure 1(b) depicts the direction of the incident beam and the geometry of the sample surface employed in the experiment. The incident beam makes an angle of 45° with the analyzer axis and data were collected at about normal emission. The outgoing electrons were analyzed using an SES-2002 analyzer followed by a 2D-CCD detector. All the ARPES experiments were performed at room temperature (RT) using a 14° angular window of the analyzer with an angular resolution better than 0.2°. The binding energies of the photoemission spectra were calibrated to the Fermi level position of the thick Ag-covered $MoS_2$ samples.

The natural $MoS_2$ single crystal (SPI Supplies, USA) was cleaved *in situ* at RT in a vacuum better than $5 \times 10^{-10}$ mbar. High purity Ag (99.999%) was deposited on the $MoS_2$ surface using an electron-beam evaporator at a rate of 2 Å/min, calibrated using a water-cooled quartz crystal thickness monitor, for details see the Supplemental Material [35]. The thickness of 1 monolayer (ML) Ag along the (111) direction is taken as 2.36 Å. The deposition was held at RT for 20 min (coverage of 40 Å, i.e., about 17 MLs) to obtain a considerable

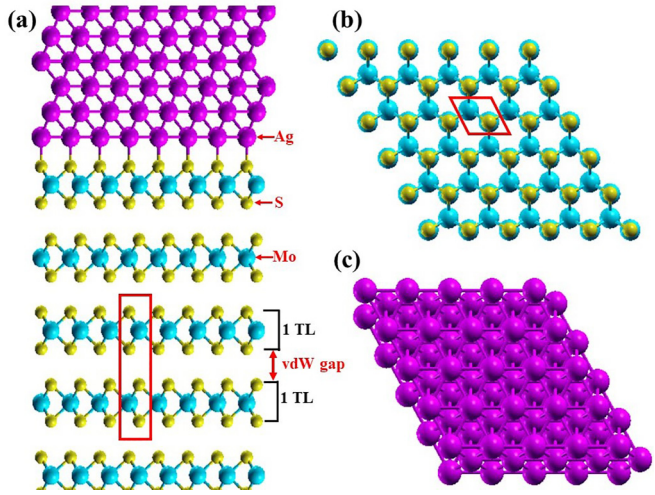


FIG. 2. (a) Schematic diagram of the side view of the Ag(111)/$MoS_2$(0001) system with the vdW gap. (b) and (c) Top view of a clean $MoS_2$(0001) surface and the Ag(111)/$MoS_2$(0001) surface, respectively. A schematic of the side and top view of the bulk 2H-$MoS_2$ unit cell is represented through a red rectangle and rhombus in (a) and (b), respectively. See text for details.

thickness so that the quantized electronic states become well visible. Our low-energy electron diffraction (LEED) studies [21,35] have shown that the Ag film on $MoS_2$(0001) substrate grows with (111) orientation with its natural lattice constant. Despite the lack of lattice matching between Ag(111) and $MoS_2$ surface, the epitaxy of the Ag film is excellent due to the interfacial vdW force as ascertained from the presence of Ag(111) surface state (SS) and detailed LEED studies [21,35]. The first Brillouin zone (BZ) and the different high symmetric directions of the substrate surface and the overlayer Ag film are depicted in Fig. 1(a).

### B. Calculation details

We have performed first-principle-based DFT calculations using the PWSCF code of the QUANTUM ESPRESSO distribution [36]. The valence electrons were described explicitly using a plane-wave basis set with cutoffs of 60 and 600 Ry for the wave functions and charge densities, respectively. The core and valence electron interactions were described by using ultrasoft pseudopotentials [37]. The exchange-correlation functional was taken into account by using a generalized gradient approximation of the Perdew-Burke-Ernzerhof form [38].

For bulk 2H-$MoS_2$ (space group $P6_3/mmc$), the energy-optimized lattice parameter and vdW-bonding distance are found to be $a = 3.16$ Å ($c = 12.48$ Å) and 3.12 Å, respectively, which is in good agreement with the experimental data [39] and earlier theoretical reports [40,41]. The clean 2H-$MoS_2$(0001) surface was constructed using a seven triple layers (TL) thick slab with $(1 \times 1)$ surface unit cell (see Fig. 2). Here we define one monolayer as 1 TL that contains 1 Mo atom layer and 2 S atom layers, and the adjacent TLs are held together through weak vdW interaction [42] between them. To take into account the vdW interactions in the DFT calculations, we have used the vdW D3 correction as proposed by Grimme [43]. The BZ sampling for bulk $MoS_2$ and $MoS_2$(0001) surface was done by using $(24 \times 24 \times 8)$ and $(18 \times 18 \times 1)$ Monkhorst-Pack (MP) $k$-point meshes, respectively.

To investigate the Ag(111)/$MoS_2$(0001) system, we have considered 18 ML thick Ag layers on top of a $(1 \times 1)$ surface unit cell of the substrate. As Ag (111) (2.89 Å) grows on $MoS_2$(0001) (3.16 Å) in a strain-relieved mode [21], for computational purposes, we have used the substrate with the same lattice parameter as the overlayer film. Similar approaches have been used in the literature for the computational modeling of systems with significant lattice mismatches between the film and substrate [44,45]. Such an expansion of the in-plane lattice constant of $MoS_2$ is found to decrease the band gap mainly through the shifting of the bottom of the conduction band while the top of the valence band is not significantly affected [46]. To obtain the preferred height of Ag islands on the $MoS_2$ surface, Kidd *et al.* [47] used freestanding Ag(111) films in their DFT calculations, but here we are not using the free-standing Ag layers as it underestimates the effect of hybridization with the substrate bands at the interface and, as a consequence, the in-plane band dispersion gets modified [48]. In our calculation we have used the optimized lattice constant for Ag(111) surface which is 2.94 Å, which is in good agreement with the earlier calculated reports [49,50].

The surface is constructed with a 16 Å wide vacuum region along the direction normal to the surface of the slab ($z$ direction) to eliminate the interactions between the artificial periodic images. To compensate for the artificial electric field appearing from the asymmetric construction of the slab, a "dipole correction" term [51] was used in our calculations. Except for the bottom-most 3 TLs, all the atoms were allowed to relax using the Broyden-Fletcher-Goldfarb-Shanno (BFGS) algorithm [52], until all components of the forces on all atoms were less than 0.001 Ry/bohr. The convergence criteria were achieved by using Marzari-Vanderbilt cold smearing [53] with a width of 0.002 Ry.

## III. RESULTS AND DISCUSSIONS

### A. Clean $MoS_2$(0001) surface

Figure 3(a) depicts the experimental $k$-resolved electronic band dispersion of cleaved $MoS_2$(0001) surface along the $\bar{\Gamma}$-$\bar{K}$ high-symmetry direction using He $II_\alpha$ photons. The valence band maximum (VBM) is located at 0.56 eV below $E_F$ at $\bar{\Gamma}$ position, indicating the surface band bending characteristics of the $n$-type semiconductor sample. The band structure exhibits a symmetric behavior around the $\bar{\Gamma}$ point while the overall dispersive features are consistent with the previous ARPES studies [40,41,54]. Figure 3(b) shows the DFT calculated band structure of bulk $MoS_2$ (blue line) and 7 TLs $MoS_2$(0001) surface (red line) along the $\Gamma/\bar{\Gamma}$-$K/\bar{K}$ high-symmetry direction. The calculated band structure is in good agreement with the experimental spectra both in energy and dispersion characteristics. The calculated band structure of $MoS_2$(0001) surface presents an indirect band gap of 1 eV involving the VBM at $\bar{\Gamma}$ point and the conduction band minima at about 0.55 $\bar{\Gamma}$-$\bar{K}$ while a direct band gap of 1.7 eV appears at $\bar{K}$ point. In the case of surface calculation, the

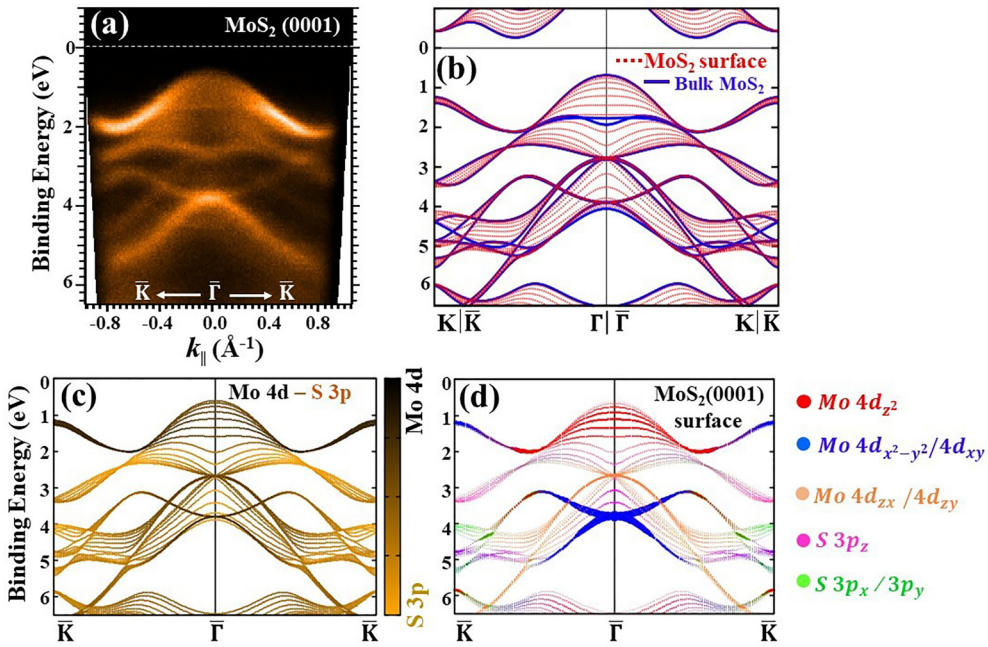


FIG. 3. (a) ARPES spectra measured with He II$_\alpha$ photons along the $\bar{\Gamma}$-$\bar{K}$ symmetry direction. (b) Calculated band structure of bulk $MoS_2$ (blue) and 7 TLs $MoS_2$(0001) surface (red dotted line). (c) Comparative contribution of S 3$p$ (orange) and Mo 4$d$ (black) orbitals of the $MoS_2$(0001) surface band structure. (d) Orbital projected Mo 4$d$ and S 3$p$ band structures of $MoS_2$(0001) surface. The colors denote the different orbitals of S 3$p$ and Mo 4$d$ states. The symbol size is proportional to the spectral weight [50] of the state.

energy state gets split up as a function of the number of layers. Thus, for the 7 TL $MoS_2$ surface (present calculation), the energy is split up into seven states, as clearly observed in the VBM [see Fig. 3(b)]. Though with the increasing number of layers the energy states get split up more, all the split states remain within the bulk band projected region.

To understand the orbital origin of the band texture, the orbital projected band structures are calculated for Mo 4$d$ and S 3$p$ states of $MoS_2$(0001) surface and are shown in Figs. 3(c) and 3(d). Figure 3(c) represents a comparative band structure of Mo 4$d$ (black) and S 3$p$ (orange) orbitals and indicate a strong Mo 4$d$-S 3$p$ hybridization. In Fig. 3(d), different colors denote the different suborbitals of S 3$p$ and Mo 4$d$ states with the size of the symbols proportional to the spectral weight [50] of the orbital states. We observe the states around the VBM originating from the out-of-plane Mo $d_{z^2}$ orbitals, whereas the states around $\bar{K}$ are coming from the in-plane Mo $d_{x^2-y^2}$ and Mo $d_{xy}$ orbitals. Furthermore, the valley-shaped dispersing band at $\bar{\Gamma}$ point, 2.0 eV below $E_F$, is notably appearing from the S 3$p_z$ orbitals while the chevron-shaped band around 3 eV is due to Mo $d_{xz}$ and Mo $d_{yz}$ orbitals. Another intense band observed at $\Gamma$ point, 3.9 eV below $E_F$, is originating from the Mo $d_{x^2-y^2}$ and Mo $d_{xy}$ orbitals.

In $MoS_2$ surface calculation, the band structure gets modified with the number of layers as a consequence of the quantum confinement and also due to the hybridization of S 3$p$ and Mo 4$d$ orbitals [7]. In our DFT calculation, it is observed that the splitting of the states near $\bar{\Gamma}$ is more compared to that at $\bar{K}$. As the electronic structure is strongly correlated with the atomic structure, the observed splitting can be attributed to the different degrees of interlayer coupling strength. As the valence electronic states near $\bar{K}$ are mainly from the localized 4$d$ orbitals of the Mo atoms, they experience less effect by the interlayer coupling as Mo atoms are located in the middle of the S-Mo-S sandwich layer. On the other hand, the states near $\bar{\Gamma}$ are originating from the hybridization of the S 3$p$ and Mo 4$d$ orbitals, they experience relatively strong interlayer coupling effects. Therefore, as the number of layers gets reduced, the top of the VBM at $\bar{\Gamma}$ shifts to higher binding energies with increasing indirect band gap width while the direct band gap remains almost unchanged and, at the monolayer limit, the indirect to direct band gap crossover is reached.

### B. Quantum states

The experimental ARPES image obtained from the Ag thin film grown on $MoS_2$(0001) substrate at a coverage of 17 ML is shown in Fig. 4(a). The data are obtained using 60 eV $p$-polarized photons along the $\bar{\Gamma}$-$\bar{K}$ direction of the Ag(111) surface BZ [see Fig. 1(a)]. After the deposition of Ag on the $MoS_2$ surface, it is observed that the VBM shifts away from the Fermi level ($E_F$) by about 300 meV [see Fig. 4(a)]. This energy shifting is arising from the formation of a Schottky barrier at the metal-semiconductor interface [54,55]. After deposition, we also observe the formation of new electronic states in the band gap region of $MoS_2$, extending from the $E_F$ to the deep valence band region. The intense band just below $E_F$ is the Ag(111) SS, whereas the discrete parabolic states at higher binding energies are interpreted as QWS/QWRS based on phase shift quantization [56]. For brevity, here we address both QWS and QWRS as quantum states. The origin of the discrete quantum states is due to electron confinement by the barrier potential that appeared at film/substrate and film/vacuum interfaces. The QWS are mainly confined within the fundamental band gap region of the substrate, while the

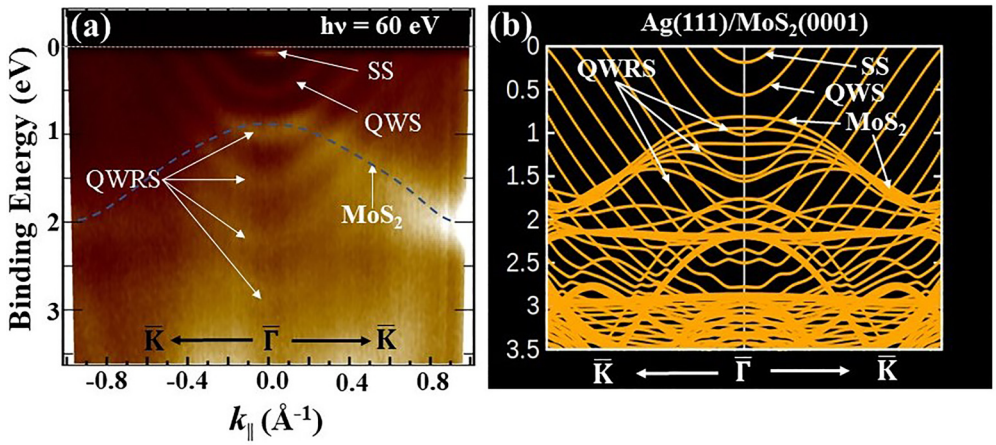


FIG. 4. (a) ARPES data obtained from 17 ML thick Ag(111) film on $MoS_2$(0001) crystal substrate at RT using photon energy of 60 eV. The dashed line indicates the dispersion of the topmost $MoS_2$ valence band. (b) The DFT calculated band structure of an 18 ML thick Ag(111) film on a strained $MoS_2$(0001) substrate surface.

QWRS gets hybridized with the underneath substrate bands. The energy position of these quantum states is governed by the Bohr-Sommerfield quantization condition, which is given by

$$2k_{\perp}(E)d + \delta(E) = 2n\pi, \tag{1}$$

where $d$ is the thickness of the quantum well, $k_{\perp}$ is the perpendicular component of the electron wave vector of the Ag(111) surface, $\delta$ is the total phase shift at the Ag-$MoS_2$ and Ag-vacuum interfaces, $E$ is the electron energy, and $n$ is an integer quantum number. Each parabolic spectrum (except SS) in Fig. 4(a) corresponds to an integer quantum number $n$. The presence of sharp QWS and SS suggests the very high structural quality of the grown film and its surface ordering. Formation of the QWS are well described by the phase accumulation model but for the QWRS, due to partial penetration of the electronic states into the substrate bands region, the total phase of the wave functions changes and as a consequence the energy position of the quantum states gets modified [57]. In our earlier work [21] we have shown that a good description of the QWRS can be obtained from the structure plots considering the quantum number-dependent total phase shifts estimated from the ARPES data.

It is clear from Fig. 4(a) that the quantum states are intense and well resolved above the $MoS_2$ band edge and become blurred for higher binding energies and can be described in terms of different degrees of electron confinement [58]. Within the band gap region, the electrons are well confined by energy conservation, while below the band edge the electrons are only partially reflected from the Ag-$MoS_2$ interface resulting in much weaker confinement forming the QWRS. It is also observed that the intensity of these quantum states decreases for off-normal emission, which can be understood in terms of the finite lateral coherence length of these states [59]. This is because the quantum states appear resulting from the interference between two waves arising from the multiple bounces between two film boundaries and the interference is strongly dependent on the coherency between these waves.

The DFT computed band structure of 18 ML Ag(111) film on $MoS_2$(0001) substrate along the $\bar{\Gamma}$-$\bar{K}$ direction is shown in Fig. 4(b). We observe a very good matching of the binding energy (BE) position as well as the dispersion characteristics of the quantum states between the calculated band structure for 18 ML Ag(111) film and the experimental ARPES spectra for a coverage of 17 ML Ag(111) film. Recent studies on the growth morphology of Ag(111) films on $MoS_2$(0001) substrate using scanning tunneling microscopy (STM) has revealed that the Ag overlayers form atomically flat surfaces with a preferred thickness of 6, 10, 14, 18, and 22 atomic layers, due to quantum size effect, is called "magic height" [60,61]. The good agreement between the experiments and calculations shown in Fig. 4 is consistent with the magic height of 18 ML, suggesting that at least 75% of the film is 18 ML thick.

Comparing the calculated and experimental spectra, we can clearly distinguish between the QWS and QWRS in the system. The Ag-derived bands that do not cross with the substrate $MoS_2$ bands are the QWS while the Ag-derived bands that do cross and mix with the $MoS_2$ bands display the QWRS character. So, for the QWRS, the Ag $p$ states are mainly getting hybridized with the Mo $d_{z^2}$ and S $p_z$ orbitals. Thus, from Fig. 4 we can say that any Ag bands that come above the valence band maximum (VBM) of the $MoS_2$ surface (−0.9 eV BE) will form the QWS, while the Ag states with BE below the VBM forms the QWRS in the system. When the energy of the QWS is within the band gap region of $MoS_2$, the state gets well trapped within the epitaxial layer. Therefore, in this surface deposition process, 2D conduction channels (QWS) emerge on the semiconducting surface and, as a consequence, the electronic behavior of the substrate gets modified dramatically. This aspect may be utilized for quantitative control of the electronic properties of these quasi-2D materials and could have important implications for future nanoelectronic devices [22].

### C. Photon energy dependence

The 2D nature of the observed quantum states is confirmed by the photon energy-dependent ARPES experiments. By changing the incident photon energy, we can tune the momentum along the film's normal direction ($k_z$) and,

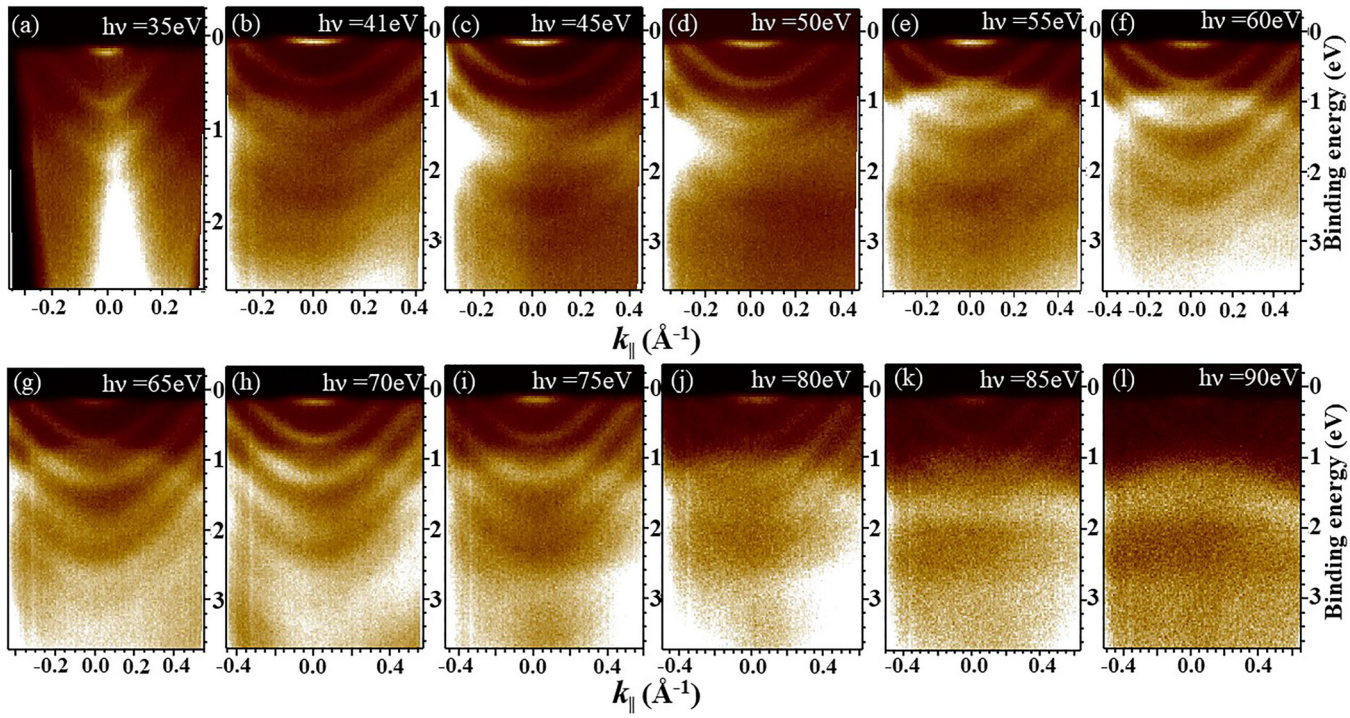


FIG. 5. Photon energy-dependent surface electronic structure of the Ag/$MoS_2$ system. The photon energy is varied from 35 to 90 eV and can observe Ag SS and quantum states in the whole photon energy range. The intensity of these electronic states varies with incident photon energy resulting from the photoemission cross-section effects. See text for details.

consequently, can obtain band dispersions containing bulk contributions that get changed as a function of incident photon energy. Figure 5 shows the ARPES spectra for diffident photon energies from 35 to 90 eV where both Ag(111) SS and the quantum states are visible in the whole energy range. To quantify the dispersion of the energy states, the energy distribution curve at the zone center ($\bar{\Gamma}$) for different photon energies is shown in Fig. 6. For Ag SS as well as for the quantum states, except for their relative intensity or spectral weight, the band dispersion does not change with the photon energy indicating the pure 2D character of these Ag(111)-derived states.

Interestingly, we can observe in Fig. 5 that the quantum states show different behavior below and above ∼1.0 eV. For lower BEs, these quantum states are very clear with high contrast, while for higher BEs they appear diffused and smudged due to hybridization with the underlying $MoS_2$ substrate states, allowing a clear distinction between the QWS and QWRS. For higher photon energies, the intensity of these quantum states decreases drastically due to the steep fall in the photoemission cross section of the Ag states [62] in this range. It is also observed that the VBM of the underlying substrate gets prominent above 55 eV photon energy and the intensity diminishes with increasing photon energy. But, for photon energies above 80 eV, the band near 2 eV BE (S $3p_z$) becomes prominent. This is because the atomic polarization cross section falls considerably for the Mo $4d$ orbitals, but for the S $3p$ orbitals, it is still higher for 80 eV and above [63]. Although the quantum states are visible in the whole photon energy range, we find 60–70 eV photons are most favorable for study due to the sharp intensity and clear visibility of dispersive bands in the ARPES spectra.

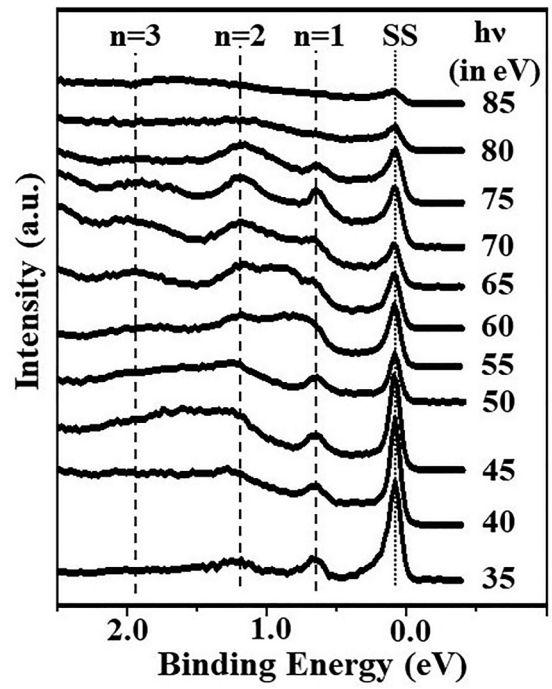


FIG. 6. Photon energy-dependent normal emission spectra of the Ag/$MoS_2$ system. The photon energy varies from 35 to 85 eV. SS represents the Ag(111) surface state. $n = 1, 2, 3$ represents the quantized Ag quantum states.

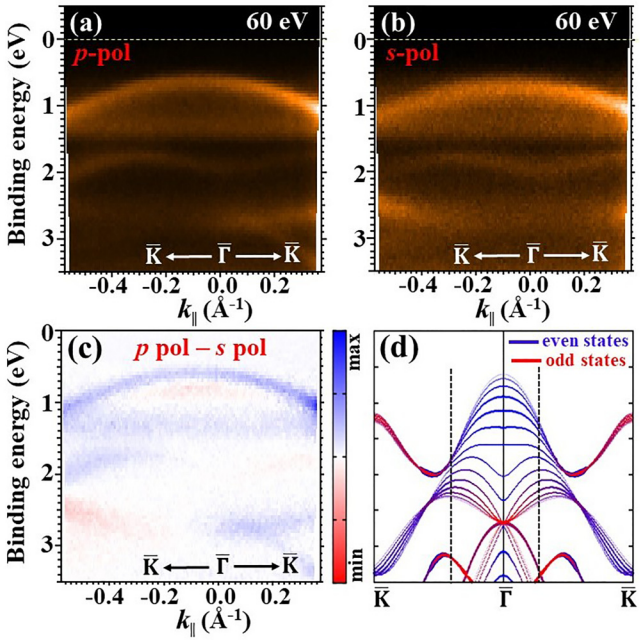


FIG. 7. (a) $p$ and (b) $s$ polarization-dependent ARPES spectra of clean $MoS_2(0001)$ surface at $h\nu = 60$ eV [64]. (c) Linear dichroism (LD) ARPES spectra of the clean $MoS_2$ surface. (d) DFT computed projected band structure for even and odd orbital states of Mo and S atoms. The black dashed line indicates the experimentally probed region in the left panel. See text for details.

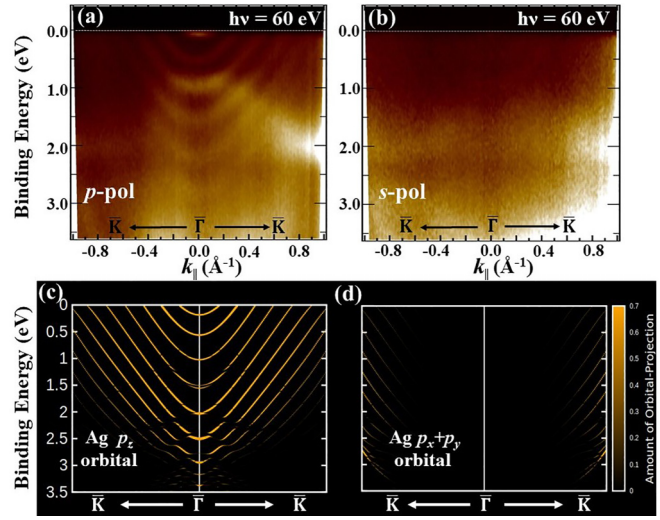


FIG. 8. (a) $p$ and (b) $s$ polarization-dependent ARPES spectra of the $Ag/MoS_2$ system at $h\nu = 60$ eV. (c) and (d) DFT computed projected band structure of Ag for out-of-plane ($p_z$) and in-plane ($p_x$ and $p_y$) orbitals, respectively.

### D. Linear polarization dependence

Figures 7(a) and 7(b) show the linear polarization-dependent ARPES spectra of clean $MoS_2(0001)$ surface along the $\bar{\Gamma}$-$\bar{K}$ direction, obtained with $h\nu = 60$ eV. From one panel to another, the relative intensities of the ARPES spectra change when the linear polarization is switched from $p$ to $s$ type, but the BE of the photoemitted states remains constant. For a quantitative view of the linear dichroism (LD), the difference between $p$-pol and $s$-pol ARPES spectra ($LD = I_{p\text{-pol}} - I_{s\text{-pol}}$) is plotted in Fig. 7(c) with a color representation, where blue and red represent the positive and negative value of LD. According to the matrix element effect [28], for $p$-polarized light the intensity of the out-of-plane orbitals gets strongly enhanced, while for $s$-polarized light the intensity of the in-plane orbitals will be dominant. But, for $MoS_2(0001)$ surface, the band symmetry along the $\bar{\Gamma}$ to $\bar{K}$ line would not be expected *a priori* because no true mirror symmetry plane exists along this direction, as the surface has a $C_{3v}$ symmetry, not $C_{6v}$ symmetry [41,54].

Figure 7(d) shows the surface projected band structure obtained for nominally even (blue) and odd (red) states with respect to the $\bar{\Gamma}$-$\bar{K}$ mirror symmetry plane. Here $s$, $p$, $d$ orbitals are represented with angular momentum quantum number $l$ and magnetic quantum number $m$ as $[l = 0, m = 0(s)]$, $[l = 1, m = -1(p_y), 0(p_z), 1(p_x)]$, and $[l = 2, m = -2(d_{xy}), -1(d_{zy}), 0(d_{z^2}), 1(d_{zx}), 2(d_{x^2-y^2})]$. We sum up all the projections corresponding to even ($m = 0, 1, 2$) and odd ($m = -1, -2$) reflection symmetries with respect to the mirror plane along the $\bar{\Gamma}$-$\bar{K}$ line. Based on the symmetry assignment, the calculated band structure exhibits a difference between the even and odd states [see Fig. 7(d)], which indicates that the weight of the spectral function depends on the wave vector of the orbitals. From the orbital projected band structures [see Fig. 3(d)], it is clear that the VBM near $\bar{\Gamma}$ has a predominant Mo $4d_{z^2}$ orbital with even state character. The valley-shaped band near 2 eV BE also exhibits the even state character as it is originating from the S $3p_z$ orbital while the electronic states at around 3 eV exhibit mixed states of even and odd symmetries. We note the reasonable agreement between the experimental and DFT computed band dispersions for both even and odd symmetry states, suggesting the applicability of the photoemission selection rules despite the lower symmetry along the $\bar{\Gamma}$-$\bar{K}$ line.

Figures 8(a) and 8(b) show the ARPES spectra for Ag on $MoS_2(0001)$ surface with $p$- and $s$-polarized light, respectively. For $p$-polarized geometry [see Fig. 1(b)], the quantum states exhibit a strong spectral weight while for the $s$-polarized geometry, the quantum states are nearly absent [65]. The electronic band structure of Ag in the BE region considered here consists of $5s$ and $4p$ orbitals as the fully filled $4d$ orbitals lay below. The $p_x$ and $p_y$ orbitals are in-plane while the $p_z$ orbital is oriented along the surface normal direction of the Ag(111) film. In an ARPES experiment, the amplitude of the photoemission matrix element strongly depends on the cross section of the electric field (**E**) and the spatial distribution of the orbital wave functions [66]. For $p$-polarized light, the **E** field points out-of-plane, therefore it exhibits a strong ARPES cross section for $p_z$ orbital as it is out-of-plane and a weak cross section for in-plane orbitals. Similarly, for the $s$ polarized light, the cross section is higher for the in-plane orbitals and weak for the out-of-plane orbitals. Therefore, the observed results in Fig. 8 indicate that the Ag-derived quantum states have a predominant $p_z$ orbital character. For a direct comparison with the DFT calculations, we obtain the orbital projected band structure (top three surface atomic layers) of the 18 ML $Ag/MoS_2$ system for out-of-plane ($p_z$) and in-plane ($p_x$ and $p_y$) orbitals, as shown in Figs. 8(c) and 8(d),

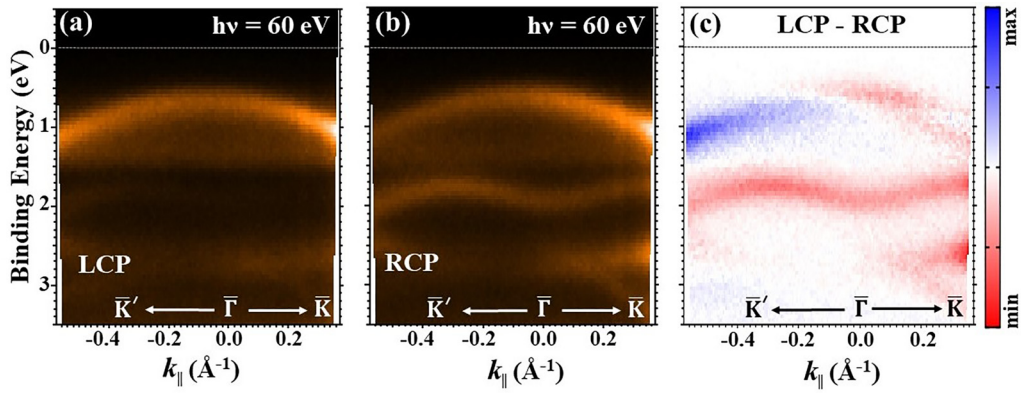


FIG. 9. (a) and (b) ARPES mapping of clean $MoS_2(0001)$ surface using circularly polarized photons of 60 eV. LCP and RCP represents left and right circularly polarized photons, respectively. (c) CD spectra ($CD = I_{LCP} - I_{RCP}$) of clean $MoS_2(0001)$ surface.

respectively. The spectral weight of the projected band structure shows that the Ag quantum states are mainly originating from the $p_z$ orbitals near the zone center, while near the zone boundaries the $p_x/p_y$ orbitals also contribute significantly.

### E. Circular polarization dependence

We have also performed the circular dichroism (CD) ARPES mapping of the clean $MoS_2(0001)$ and $Ag/MoS_2(0001)$ samples using the RCP/LCP light at a photon energy of 60 eV. The ARPES images of the $MoS_2(0001)$ surface using LCP and RCP photons are shown in Figs. 9(a) and 9(b), respectively, while the extracted CD image is shown in Fig. 9(c). The magnitude of the circular dichroism is given by $CD = I_{LCP} - I_{RCP}$ where $I_{RCP}$ and $I_{LCP}$ are the photoemission intensities obtained for the right and left circularly polarized lights, respectively. It is observed that for the clean $MoS_2$ surface, the topmost valence band exhibits an intensity asymmetry between the left and right sides of $k_\parallel = 0$ Å$^{-1}$ as the CD signal reverse sign from $+k$ to $-k$ side. i.e., the LCP (RCP) data have higher intensity in the $k_\parallel < 0$ ($k_\parallel > 0$) region. Furthermore, the states at higher BEs, around 2 and 3 eV below the $E_F$ at $\bar{\Gamma}$ also exhibits CD behavior though they do not show any intensity asymmetry.

In the case of a monolayer of 2H-$MX_2$ TMDC, there exist inequivalent $K$ points in the BZ, $K$ and $K'$ [67], due to the broken inversion symmetry [7,15,68]. For materials with strong spin-orbit coupling, this results in the spin spitting in these inequivalent valleys at $K$ [7,15], leading to novel transport phenomena such as the valley Hall effect [68,69] which can be understood in terms of Berry curvature [68,70,71]. Circular dichroism characteristics, observed in CD-ARPES experiments on spin-orbit coupled systems, are sensitive to different factors such as initial-state spin/orbital angular momentum, final-state effects, or chirality of the experimental setup and their interpretations are often been controversial [72]. A recent study [30] has proposed that CD-ARPES could be used to map the Berry curvature distribution in the reciprocal space which could directly probe the topological character of the spin-split systems. Though we do not expect to observe CD signals from the bulk $MoS_2$ system due to the existence of inversion and time-reversal symmetry, the surface sensitivity of the ARPES helps to observe the hidden spin [14,73] and orbital angular momentum [30] that are layer locked in these materials. Our CD-ARPES result for the $MoS_2$ surface in Fig. 9 is similar to that observed for $WSe_2$ [30,31] around $\bar{\Gamma}$ region. However, a detailed description of the observed CD signal is beyond the scope of the present work as it has contributions from different factors including the exact geometry of the experimental setup.

In Figs. 10(a) and 10(b) we show the experimental ARPES images from the 17 ML Ag(111) thin film on $MoS_2(0001)$ surface using the left and right circularly polarized photons of 60 eV, respectively. For a quantitative evaluation of the ARPES spectra, energy-dispersive line scans were obtained at G ($k_\parallel = 0$ Å$^{-1}$), B ($k_\parallel = -0.3$ Å$^{-1}$), and B1 ($k_\parallel = 0.3$ Å$^{-1}$) positions (marked by yellow dotted lines) and are plotted in Figs. 10(c)–10(e), respectively. We have plotted the background-subtracted spectra to better show the dichroic effects on the ARPES spectra, which were normalized to the Ag(111) SS intensity at the $\bar{\Gamma}$ as no dichroism is expected for the SS at $k_\parallel = 0$ Å$^{-1}$ position [74]. For the QWS of the $Ag/MoS_2(0001)$ system, we do not observe any difference in the photoemission intensity between the RCP/LCP photons (i.e., no CD signal). However, for the case of QWRS, where the quantum states are getting hybridized with the substrate $MoS_2$ bands, we observe a CD signal (difference in the RCP/LCP intensity) in Figs. 10(c)–10(e). The observed CD signal from the QWRS is consistent with the CD signal observed from the substrate $MoS_2$ bands in Fig. 9(c). From Fig. 10(d) for $n = 3$ QWRS at about 1.2 eV BE, we can see that the photoemission band intensity (and the CD signal) gets reversed for the B and B1 positions ($\pm 0.3$ Å$^{-1}$) when the helicity of the incident light gets reversed. However, for the deeper QWRS such as for $n = 4$ and $n = 5$ states, we do observe a finite CD signal without any reversal in the intensity between B and B1 positions, in agreement with the CD signal from the clean $MoS_2$ surface [see Fig. 9(c)]. We observe that the CD behavior is dominant for those QWRS which are hybridizing with the topmost valence band of $MoS_2$ surface. For higher binding energies, the CD signal for the QWRS is small, but still visible in Figs. 10(d) and 10(e). Furthermore, it can also be observed that the APRES signals at the $\bar{\Gamma}$ point show a reversal of the intensities for the RCP and LCP light for $n = 1$ and 2 quantum states, which also agrees with the CD data in Fig. 9(c).

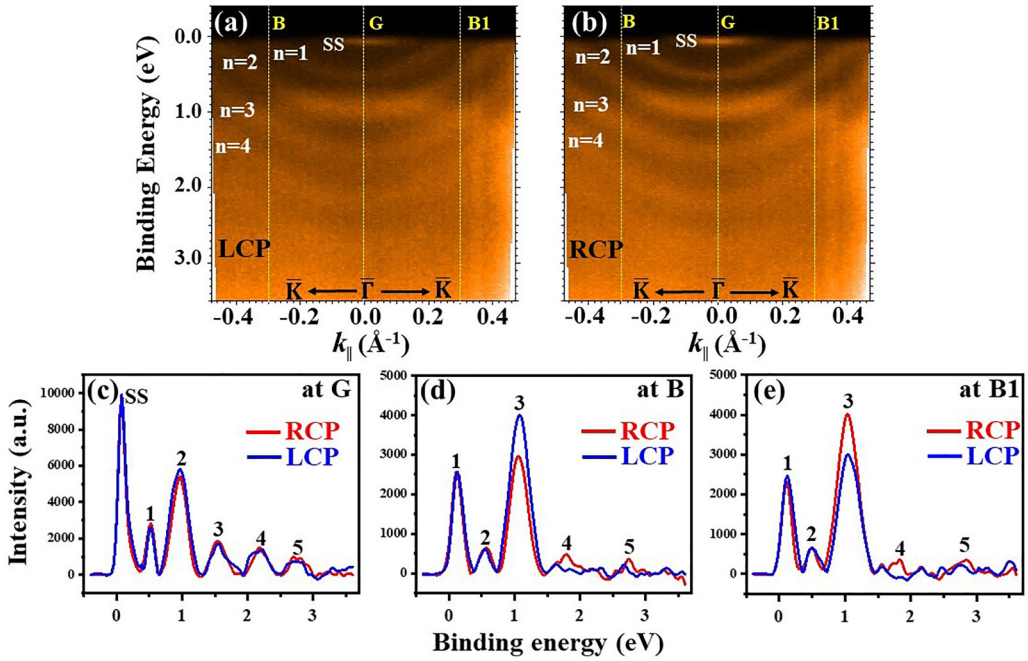


FIG. 10. (a) and (b) ARPES mapping of $Ag/MoS_2$ surface using circularly polarized photons of 60 eV. LCP and RCP represents left and right circularly polarized photons, respectively. (c)–(e) Comparison of the background-subtracted ARPES spectra obtained for LCP and RCP polarized light at $k_\parallel = -0.3$ Å$^{-1}$(B), 0.0 Å$^{-1}$(G), 0.3 Å$^{-1}$(B1), respectively. The integer number denotes the order of the corresponding quantum states.

Thus, our CD-ARPES experiments on the $Ag/MoS_2(0001)$ system show that the QWRS on the Ag film gets induced a CD effect due to the virtue of their hybridization with the substrate states while the QWS that are confined only to the Ag film does not show any induced effect. The CD effect observed on the QWRS of Ag film is found to be the same as observed on the bare $MoS_2(0001)$ surface. For a detailed understanding, one needs to do further experiments such as thickness-dependent studies to understand the range of these interactions. This observation might also be useful for the realization of the proposed valleytronic devices. Thus, manipulation of the orbital texture of the 2D-conduction channels (quantum states) in the overlayer film through substrate hybridization can provide new possibilities to tune their properties.

## IV. SUMMARY AND CONCLUSION

In summary, we have studied the electronic structure of clean and Ag-induced quantum states on $MoS_2(0001)$ single-crystal surfaces using photon energy and polarization-dependent ARPES experiments. Using selective linear polarization of the incident light, our ARPES experiments unambiguously identify the orbital character of the surface electronic states. Even in the absence of a true mirror symmetry plane along the $\bar{\Gamma}$-$\bar{K}$ line, the electronic band structure exhibits a significant difference for the orbital states of even and odd reflection parties. The in-plane dispersion of the Ag $p_z$ quantum states is found to be associated with electron confinement and is characterized by the phase shift quantization rule. A photon energy-dependent dispersion characteristic of the band structure exhibits 2D behavior of the quantized electronic states. The QWS is found to be well confined within the overlayer film, while the QWRS hybridize with the underlying Mo $4d_{z^2}$ and S $3p_z$ orbitals exhibit a lesser amount of electron confinement. The observed momentum-dependent intensity variation of the quantum states is a consequence of the finite lateral coherence length of the electrons. Comparison between the polarized ARPES measurements and the calculated spectral function provides detailed symmetry information on the band structure and a microscopic insight into the electronic behavior of the system. The well-confined QW states of the Ag overlayer established a 2D-channel path on the semiconducting substrate surface and drastically modifies its electronic properties, which could have significant implications for the optoelectronic devices.

Despite having inversion symmetry for the bare 2H-$MoS_2$ system, the ARPES experiments with circularly polarized light exhibit CD on the valence electronic states. Depending on the handedness of the incident circularly polarized light, we observe an intensity asymmetry around $\bar{\Gamma}$ point on the topmost valence band of the $MoS_2$ surface. As the CD behavior is only expected from the $MX_2$ monolayer, the observed results for bulk $MoS_2$ have been interpreted in the literature as the hidden spin/orbital angular momentum [14,30]. Our CD-ARPES experiments on the Ag(111) layers grown on $MoS_2(0001)$ surface showed no observable circular dichroism for the QWS confined to the Ag layers. However, the extended QWRS showed circular dichroism similar to that observed on the bare $MoS_2$ with the helicity of the incident photons, expected to be originated from the underlying substrate surface due to the hybridization between the electronic states. Thus, the quantum size effects of the thin layer film are shown to influence the spin-orbit texture of the system enabling tuning its properties.

## ACKNOWLEDGMENTS

We acknowledge the Micro-Nano Initiative program of the Department of Atomic Energy (DAE), Government of India, for generous funding and support. A.K. acknowledges the University Grant Commission (UGC), India, for the Ph.D. fellowship. We thank Prof. Shobhana Narasimhan and Arpan Das, JNCASR, Bangalore, for helpful discussions on the DFT calculational procedures.



[1] A. K. Geim and K. S. Novoselov, Nat. Mater. **6**, 183 (2007).
[2] M. Z. Hasan and C. L. Kane, Rev. Mod. Phys. **82**, 3045 (2010).
[3] Q. H. Wang, K. Kalantar-Zadeh, A. Kis, J. N. Coleman, and M. S. Strano, Nat. Nanotechnol. **7**, 699 (2012).
[4] S. Manzeli, D. Ovchinnikov, D. Pasquier, O. V. Yazyev, and A. Kis, Nat. Rev. Mater. **2**, 17033 (2017).
[5] K. Novoselov, o. A. Mishchenko, o. A. Carvalho, and A. Castro Neto, Science **353**, aac9439 (2016).
[6] S. Balendhran, S. Walia, H. Nili, J. Z. Ou, S. Zhuiykov, R. B. Kaner, S. Sriram, M. Bhaskaran, and K. Kalantar-zadeh, Adv. Funct. Mater. **23**, 3952 (2013).
[7] K. F. Mak, C. Lee, J. Hone, J. Shan, and T. F. Heinz, Phys. Rev. Lett. **105**, 136805 (2010).
[8] H. Liu, A. T. Neal, Z. Zhu, Z. Luo, X. Xu, D. Tománek, and P. D. Ye, ACS Nano **8**, 4033 (2014).
[9] B. Radisavljevic, A. Radenovic, J. Brivio, V. Giacometti, and A. Kis, Nat. Nanotechnol. **6**, 147 (2011).
[10] H. Kwon, S. Garg, J. H. Park, Y. Jeong, S. Yu, S. M. Kim, P. Kung, and S. Im, npj 2D Mater. Appl. **3**, 9 (2019).
[11] Z. Wang and B. Mi, Environ. Sci. Technol. **51**, 8229 (2017).
[12] X. Li and H. Zhu, J. Materiomics **1**, 33 (2015).
[13] S. Das, H.-Y. Chen, A. V. Penumatcha, and J. Appenzeller, Nano Lett. **13**, 100 (2013).
[14] E. Razzoli, T. Jaouen, M.-L. Mottas, B. Hildebrand, G. Monney, A. Pisoni, S. Muff, M. Fanciulli, N. C. Plumb, V. A. Rogalev, V. N. Strocov, J. Mesot, M. Shi, J. H. Dil, H. Beck, and P. Aebi, Phys. Rev. Lett. **118**, 086402 (2017).
[15] T. Cao, G. Wang, W. Han, H. Ye, C. Zhu, J. Shi, Q. Niu, P. Tan, E. Wang, B. Liu *et al.*, Nat. Commun. **3**, 887 (2012).
[16] H. Yuan, G. Cheng, L. You, H. Li, H. Zhu, W. Li, J. J. Kopanski, Y. S. Obeng, A. R. Hight Walker, D. J. Gundlach *et al.*, ACS Appl. Mater. Interfaces **7**, 1180 (2015).
[17] C. Gong, C. Huang, J. Miller, L. Cheng, Y. Hao, D. Cobden, J. Kim, R. S. Ruoff, R. M. Wallace, K. Cho *et al.*, ACS Nano **7**, 11350 (2013).
[18] K. Schauble, D. Zakhidov, E. Yalon, S. Deshmukh, R. W. Grady, K. A. Cooley, C. J. McClellan, S. Vaziri, D. Passarello, S. E. Mohney *et al.*, ACS Nano **14**, 14798 (2020).
[19] F. Wu, H. Tian, Y. Shen, Z. Hou, J. Ren, G. Gou, Y. Sun, Y. Yang, and T.-L. Ren, Nature (London) **603**, 259 (2022).
[20] E. C. Ahn, npj 2D Mater. Appl. **4**, 17 (2020).
[21] S. K. Mahatha and K. S. R. Menon, J. Phys.: Condens. Matter **25**, 115501 (2013).
[22] N. Alidoust, G. Bian, S.-Y. Xu, R. Sankar, M. Neupane, C. Liu, I. Belopolski, D.-X. Qu, J. D. Denlinger, F.-C. Chou *et al.*, Nat. Commun. **5**, 4673 (2014).
[23] I. Matsuda, T. Ohta, and H. W. Yeom, Phys. Rev. B **65**, 085327 (2002).
[24] J. H. Dil, J. W. Kim, T. Kampen, K. Horn, and A. R. H. F. Ettema, Phys. Rev. B **73**, 161308(R) (2006).
[25] J. E. Ortega and F. J. Himpsel, Phys. Rev. Lett. **69**, 844 (1992).
[26] J. E. Ortega, F. J. Himpsel, G. J. Mankey, and R. F. Willis, Phys. Rev. B **47**, 1540 (1993).
[27] A. Damascelli, Z. Hussain, and Z.-X. Shen, Rev. Mod. Phys. **75**, 473 (2003).
[28] S. Hüfner, *Photoelectron Spectroscopy: Principles and Applications* (Springer Science & Business Media, New York, 2013).
[29] W. Eberhardt and F. J. Himpsel, Phys. Rev. B **21**, 5572 (1980).
[30] S. Cho, J.-H. Park, J. Hong, J. Jung, B. S. Kim, G. Han, W. Kyung, Y. Kim, S.-K. Mo, J. D. Denlinger, J. H. Shim, J. H. Han, C. Kim, S. R. Park, Phys. Rev. Lett. **121**, 186401 (2018).
[31] S. Cho, J.-H. Park, S. Huh, J. Hong, W. Kyung, B.-G. Park, J. Denlinger, J. H. Shim, C. Kim, and S. R. Park, Sci. Rep. **11**, 1684 (2021).
[32] G. Panaccione, I. Vobornik, J. Fujii, D. Krizmancic, E. Annese, L. Giovanelli, F. Maccherozzi, F. Salvador, A. De Luisa, D. Benedetti *et al.*, Rev. Sci. Instrum. **80**, 043105 (2009).
[33] S. K. Mahatha and K. S. R. Menon, Curr. Sci. **98**, 759 (2010).
[34] M. Mulazzi, G. Rossi, J. Braun, J. Minár, H. Ebert, G. Panaccione, I. Vobornik, and J. Fujii, Phys. Rev. B **79**, 165421 (2009).
[35] See Supplemental Material at http://link.aps.org/supplemental/10.1103/PhysRevB.106.235146 for details on sample preparation and surface characterization.
[36] P. Giannozzi, S. Baroni, N. Bonini, M. Calandra, R. Car, C. Cavazzoni, D. Ceresoli, G. L. Chiarotti, M. Cococcioni, I. Dabo *et al.*, J. Phys.: Condens. Matter **21**, 395502 (2009).
[37] D. Vanderbilt, Phys. Rev. B **41**, 7892 (1990).
[38] J. P. Perdew, K. Burke, and M. Ernzerhof, Phys. Rev. Lett. **77**, 3865 (1996).
[39] W. Schutte, J. De Boer, and F. Jellinek, J. Solid State Chem. **70**, 207 (1987).
[40] S. K. Mahatha, K. D. Patel, and K. S. R. Menon, J. Phys.: Condens. Matter **24**, 475504 (2012).
[41] S. W. Han, G.-B. Cha, E. Frantzeskakis, I. Razado-Colambo, J. Avila, Y. S. Park, D. Kim, J. Hwang, J. S. Kang, S. Ryu *et al.*, Phys. Rev. B **86**, 115105 (2012).
[42] Y. Han, M. C. Tringides, J. W. Evans, and P. A. Thiel, Phys. Rev. Res. **2**, 013182 (2020).
[43] S. Grimme, J. Antony, S. Ehrlich, and H. Krieg, J. Chem. Phys. **132**, 154104 (2010).
[44] M. H. Upton, C. M. Wei, M. Y. Chou, T. Miller, and T.-C. Chiang, Phys. Rev. Lett. **93**, 026802 (2004).
[45] A. Bruix, J. A. Miwa, N. Hauptmann, D. Wegner, S. Ulstrup, S. S. Grønborg, C. E. Sanders, M. Dendzik, A. Grubisic Cabo, M. Bianchi, J. V. Lauritsen, A. A. Khajetoorians, B. Hammer, and P. Hofmann, Phys. Rev. B **93**, 165422 (2016).
[46] C. V. Nguyen, N. N. Hieu, and D. T. Nguyen, Nanoscale Res. Lett. **10**, 433 (2015).

[47] T. Kidd, J. Weber, R. Holzapfel, K. Doore, and A. Stollenwerk, Appl. Phys. Lett. **113**, 191603 (2018).
[48] A. Kar, S. K. Mahatha, and K. S. R. Menon (unpublished).
[49] G. Cipriani, D. Loffreda, A. Dal Corso, S. de Gironcoli, and S. Baroni, Surf. Sci. **501**, 182 (2002).
[50] J. Das, S. Biswas, K. Ulman, R. Banerjee, G. Gautam, A. K. Kundu, S. Narasimhan, and K. S. R. Menon, Phys. Rev. B **98**, 075137 (2018).
[51] L. Bengtsson, Phys. Rev. B **59**, 12301 (1999).
[52] R. Fletcher, *Practical Methods of Optimization* (John Wiley & Sons, New York, 1987).
[53] N. Marzari, D. Vanderbilt, A. De Vita, and M. C. Payne, Phys. Rev. Lett. **82**, 3296 (1999).
[54] T. Komesu, D. Le, Q. Ma, E. F. Schwier, Y. Kojima, M. Zheng, H. Iwasawa, K. Shimada, M. Taniguchi, L. Bartels *et al.*, J. Phys.: Condens. Matter **26**, 455501 (2014).
[55] P. E. Evans, T. Komesu, E. F. Schwier, S. Kumar, K. Shimada, and P. A. Dowben, J. Phys.: Condens. Matter **32**, 465001 (2020).
[56] I. Matsuda, H. W. Yeom, T. Tanikawa, K. Tono, T. Nagao, S. Hasegawa, and T. Ohta, Phys. Rev. B **63**, 125325 (2001).
[57] A. Shikin, D. Vyalikh, G. Prudnikova, and V. Adamchuk, Surf. Sci. **487**, 135 (2001).
[58] T. Miller, A. Samsavar, G. E. Franklin, and T.-C. Chiang, Phys. Rev. Lett. **61**, 1404 (1988).
[59] M. A. Mueller, T. Miller, and T.-C. Chiang, Phys. Rev. B **41**, 5214 (1990).
[60] T. E. Kidd, E. O'Leary, A. Anderson, S. Scott, and A. J. Stollenwerk, Phys. Rev. B **100**, 235447 (2019).
[61] C.-H.-T. Chang, H.-H. Chang, P.-C. Jiang, and W.-B. Su, Jpn. J. Appl. Phys. **57**, 08NB10 (2018).
[62] S. L. Molodtsov, S. V. Halilov, V. D. P. Servedio, W. Schneider, S. Danzenbächer, J. J. Hinarejos, M. Richter, and C. Laubschat, Phys. Rev. Lett. **85**, 4184 (2000).
[63] J. Yeh and I. Lindau, At. Data Nucl. Data Tables **32**, 1 (1985).
[64] A small asymmetry in the ARPES data is due to a slight sample tilt ($\sim 0.4^{\circ}$) present.
[65] The slight signature of QWS in *s* polarization light is due to incomplete polarization (6%) of the incident light.
[66] Y. Cao, J. Waugh, X. Zhang, J.-W. Luo, Q. Wang, T. Reber, S. Mo, Z. Xu, A. Yang, J. Schneeloch *et al.*, Nat. Phys. **9**, 499 (2013).
[67] The inequivalent *K* points are not shown in Fig. 1 and in other figures for simplicity.
[68] D. Xiao, G.-B. Liu, W. Feng, X. Xu, and W. Yao, Phys. Rev. Lett. **108**, 196802 (2012).
[69] K. F. Mak, K. L. McGill, J. Park, and P. L. McEuen, Science **344**, 1489 (2014).
[70] D. Xiao, M.-C. Chang, and Q. Niu, Rev. Mod. Phys. **82**, 1959 (2010).
[71] D. Xiao, W. Yao, and Q. Niu, Phys. Rev. Lett. **99**, 236809 (2007).
[72] M. R. Scholz, J. Sánchez-Barriga, J. Braun, D. Marchenko, A. Varykhalov, M. Lindroos, Y. J. Wang, H. Lin, A. Bansil, J. Minár, H. Ebert, A. Volykhov, L. V. Yashina, and O. Rader, Phys. Rev. Lett. **110**, 216801 (2013).
[73] J. M. Riley, F. Mazzola, M. Dendzik, M. Michiardi, T. Takayama, L. Bawden, C. Granerød, M. Leandersson, T. Balasubramanian, M. Hoesch *et al.*, Nat. Phys. **10**, 835 (2014).
[74] H. Ryu, I. Song, B. Kim, S. Cho, S. Soltani, T. Kim, M. Hoesch, C. H. Kim, and C. Kim, Phys. Rev. B **95**, 115144 (2017).